Composites Part A 126 (2019) 105597

Contents lists available at ScienceDirect

Composites Part A

journal homepage: www.elsevier.com/locate/compositesa

Dynamic characterisation of interlaminar fracture toughness in carbon fibre epoxy composite laminates

M.A. Riezzo[a,b], M. Simmons[c], B. Russell[c], F. Sket[a], V. Martínez[a,d], C. González[a,b,*]

[a] IMDEA Materials, C/Eric Kandel 2, 28906 Getafe, Madrid, Spain
[b] Departamento de Ciencia de Materiales, Universidad Politécnica de Madrid, E.T.S. de Ingenieros de Caminos, 28040 Madrid, Spain
[c] Hexcel Composites Ltd., Duxford, Cambridge CB22 4QB, United Kingdom
[d] Department of Materials Science and Engineering and Chemical Engineering, Carlos III University, 28911 Leganés, Madrid, Spain

ARTICLE INFO

Keywords:
A. Fracture toughness
B. Dynamic behaviour
B. Delamination
C. Rate dependence

ABSTRACT

In this work, the rate dependence of mode I interlaminar fracture toughness for two different materials systems, IM7/8552 and IM7/M91, both unidirectional UD carbon-fibre epoxy composite laminates have been examined over a wide range of loading rates from 0.5 mm/min up to 2000 mm/s at room temperature. Quasi-static fracture tests were performed using a DCB (double-cantilever beam) method with a screw-driven testing machine, while the dynamic tests were carried out using a WIF (wedge-insert fracture) specimen loaded dynamically in a hydraulic system. For performing the tests at high displacement rates, a special setup was designed and manufactured which allowed the insertion of the wedge within the DCB specimens at different cross-head displacement rates. The experimental technique used a pair of strain gauges attached to the bending surface of one of the arms of the cantilever beams and far from the initial crack tip. The peak values of the recorded strain were used to determine the fracture toughness under dynamic conditions through use of the compliance calibration method. A finite element model was developed to check the consistency of the measurements and validate the data reduction method used. The results exhibited rate insensitive behaviour in the case of the IM7/8552 laminates while IM7/M91 showed the contrary behaviour with maximum peak at 500 mm/s of displacement rate, with a toughness increase of ≈ 95% with respect to the quasi-static conditions.

1. Introduction

The use of polymer-based composite materials in aircraft structures has increased consistently in the last decades and today they represent up to 50% in weight for wings, fuselage sections and tail surfaces in the latest generation of commercial aircrafts [1–4]. However, the use of such composites in other parts of the aircraft that could benefit from their low weight, such as the fan blades of engines and nacelles, is progressing, but at more subdued rate. It is highly likely that this latter use could be partially attributed to the lack of a general knowledge regarding the mechanical response of composite laminates under dynamic loading or impact [5]. In order to exploit the composite mechanical performance, it is necessary to characterize the laminate and its constituents in a wide range of strain-rate conditions.

Delamination is one of the most common and critical failure modes in composite materials when loaded by a dynamic impact event [6–8]. It can produce detrimental reductions of the stiffness and residual strength of the material without obvious damage, often termed as barely visible damage (BVID) [9]. Loading-rate effects on the delamination of composite materials have been a matter of research in the scientific literature during the last decades [10–18]. With regard to delamination assessment, standard DCB testing has been extensively used although flexural inertia effects and large asymmetric loading of the arms becomes a limitation specially for rates in excess of 0.5 m/s [19,20]. Load introduction by the Wedge-Insert Fracture method (WIF) can be used to mitigate such dynamic effects, allowing the propagation of the crack under mode I rather than the mix mode observed in DCB specimens. In addition to such problems, there are also experimental difficulties associated with the direct measurement of the crack length during the dynamic tests which is a variable required in data reduction methods based on the fracture area determination [12,14,21,19]. The dynamic initiation fracture toughness of S2/8552 and IM7/977-3 composite systems were studied through using WIF methods coupled with Hopkinson split bars reaching propagations speeds as high as 1000 m/s [22]. In his review May [23] establishes that the Wedge Loaded Double Cantilever Beam test is the best suitable for measuring

* Corresponding author.
E-mail address: carlosdaniel.gonzalez@imdea.org (C. González).

https://doi.org/10.1016/j.compositesa.2019.105597
Received 24 May 2019; Received in revised form 16 July 2019; Accepted 19 August 2019
Available online 21 August 2019

the mode I fracture toughness for moderate and high loading rates. Among different reasons, specimen symmetric opening is enforced as well as the easiness of manufacturing, although care must be taken to consider the friction between the inserted wedge and the specimen. Thorsson et al. [24] suggested the use of a modified wedge-insert fracture (MWIF) in which the load is introduced by driving a triangular wedge between rollers attached to the specimen arms removing the problem of friction between the wedge and the crack surfaces.

Due to the notable degree of complexity found in the dynamic testing of interlaminar toughness of composite laminates, the results published in the literature showed significant discrepancies without a clear explanation of either the strain-rate effects or the associated fracture mechanisms [25]. In their review, Cantwell and Blyton [26] indicated that the rate sensitivity of UD CFRP was dominated by the toughness of the matrix. With a brittle matrix, composites exhibited much less of a rate effect than tough matrix composites. However they did not suggest any reason why such different result had been obtained by different workers on similar material. Some researchers reported initiation toughness increasing with loading rate [12,15,16,18], while others have contradicted these findings [14,13]. For instance, Kusaka et al. [10,11] have dedicated effort and resources to developing experimental methods for estimating the fracture toughness under impact loading using the previously described WIF methodology. These authors demonstrated that, for a first generation composite material with brittle epoxy resin, the fracture toughness decreased stepwise with increasing loading rate only in the range between 0.05 mm/min and 5 mm/min while the behaviour was almost rate-insensitive above this speed range. Aliyu and Daniel [15] used DCB specimens to study the effect of loading rate on fracture toughness of AS-4/3501 carbon/epoxy composites. At the lower loading rates, crack extension was monitored visually; while at higher rates, it was monitored by strain gauges mounted on the surface of the specimen or on a conductive paint circuit attached to the edge of the specimen. A 28% increase in the critical strain energy release rate, G_{Ic}, was observed over three orders of magnitude of loading rate. You and Yum [21] reported a 73% increase in the mode I interlaminar fracture toughness of brittle carbon/epoxy composite with increasing loading rate from 2 to 120 mm/s. During their studies, Benmedakhene et al. [12] used DCB specimens tested in universal frame at displacement rates of 2, 100 and 500 mm/min and used a simple-cantilever beam (SCB) for dynamic tests in the range of 1–5 m/s in a drop-weight impact tester. The composite used in this study was Epoxy M10 resin (Vicotex) reinforced with 52% E-glass fibers. The experimental results obtained by these authors showed a consistent increase of G_{Ic} as a function of the applied velocity. The authors concluded that the resin became brittler as the velocity increased providing an explanation of the changes in the fracture mechanisms as a function of the applied velocity: at low speed, failure propagates principally in the resin layer between the plies, and progressively as the velocity increases, the failure propagates into the fiber/matrix and interply interfaces. Zabala et al. [13] performed DCB tests from 8.3×10^{-5} to 0.19 m/s, measuring crack length and specimen opening displacement through use of a high speed camera. The materials studied in this case were unidirectional and woven (plain weave) high-strength plain carbon fibre composite using a bi-component epoxy matrix system processed by vacuum infusion. Results over the displacement rate analyzed have shown an interlaminar fracture energy reduction of $\approx$ 20% for woven reinforcement, and $\approx$ 30% in the case of unidirectional laminates. These authors hypothesize that the reduction could be attributed to a change in the crack growth behaviour from the quasi-static to dynamic tests, which in fractographic analysis is documented as less fibre/matrix interface failure and brittler matrix cracking. All these studies present evidence of different behaviours seen in similar material systems as a function of the loading rate. It is still unclear what should be the expected trend in fracture toughness as the rate is increased, and as to what are the underlying mechanisms. Normally, it was assumed that changes in fracture mechanisms are responsible for the variations of the fracture toughness measured with the aforementioned methods.

The purpose of this work is to characterize the rate dependence of mode I interlaminar fracture toughness in two different materials systems, 8552/IM7 and M91/IM7, both unidirectional UD carbon-fibre epoxy composite laminates, over a wide range of loading rates from quasi-static (displacement rate, $\dot{\delta} = 0.5$–450 mm/min) to moderate rates ($\dot{\delta} = 500$–2000 mm/s). Materials and experimental techniques are summarized in Section 2. DCB and WIF tests are performed for quasi-static and dynamic conditions. WIF tests were performed following the original work developed by Kusaka et al. [10] and employed to provide accurate measurement of the fracture toughness under dynamic conditions. A description of the data reduction method used in the work is presented in detail. Section 3 contains the experimental results carried out, including the fracture toughness rate dependence as well as an investigation of the fracture mechanisms by means of scanning electron microscopy (SEM) and X-ray computed tomography (XCT). An increase in the interlaminar toughness was detected for IM7/M91 system while for the IM7/8552 the interlaminar fracture toughness was constant in the displacement rate range considered. Changes in the fracture mechanisms were found to be a possible reason of the toughness variation of the IM7/M91 system. A finite element model was developed in Section 4 and used to validate the WIF methodology supporting the experimental results. Lastly, some remarks and conclusions are drawn in Section 5.

2. Materials and experimental techniques

2.1. Materials and specimen preparation

Two unidirectional UD carbon fiber reinforced polymer laminates were studied in this work, sharing the same type of carbon fiber IM7 (Hexcel HexTow) and two different epoxies resins, namely, Hexcel 8552 and M91. Both materials exhibited different behaviour under dynamic and impact loading. The 8552 resin is an amine-cured epoxy containing polyethersulphone as toughening agent while M91 is a high-toughness epoxy resin containing polyethersulphone and thermoplastic interleaf particles. Prepreg materials IM7/8552 and IM7/M91 belong to the second and third generations of materials used for aerospace primary structures construction, respectively. Panels following the $[0°]_4$, $[90°]_8$ and $[\pm 45°]_{4s}$ stacking sequences were prepared for longitudinal tension, transverse tension and in-plane shear tests according to ASTMD3039, EN2597:1988 and AITM 1-0002 standards, respectively. In addition, $[0]_{12}$ panels were also prepared to perform interlaminar fracture toughness tests according to ASTM D5528 standard. These latter specimens contained 25 μm thick polytetrafluoroethylene (PTFE) Teflon film inserted in the mid-plane to act as an artificial crack starter. All the panels were cured following the cycle recommended by the manufacturer through using a 180°C hold for 135 min while cooling and heating rates were constrained to 2°C/min.

Tension tests on $[0°]_4$, $[90°]_8$ and $[\pm 45°]_{4s}$ coupons were carried out using an Instron 5966 screw-driven universal testing frame with the cross-head speed ranging between $\dot{\delta} = 0.5$ and 450 mm/min. The strain in these tests was recorded with an iMetrum XT-202 video extensometer with extension resolution of 0.12 μm. The specimens were first sprayed with a white paint. Then black dots were painted to create the speckle pattern necessary for strain measurement. The strain-rate in these tests was calculated from the slope of the curve $\epsilon(t)$ recorded by the video extensometer.

DCB specimens [27,28] are commonly used to determine experimentally the mode I interlaminar fracture toughness G_{Ic} in composite laminates. The geometry used follows the ASTM D5528 standard as shown in Fig. 1(a) using the $[0]_{12}$ panels with nominal thickness of $2h = 3$ mm. Paralepipedic specimens of length $L = 250$ mm, width $b = 25$ mm were machined in the direction of the fiber using a water-cooled milling machine. The initial crack length was set to $a_0 = 25$ mm. An initial pre-crack of $\approx 2 - 3$ mm is introduced in all the specimens to

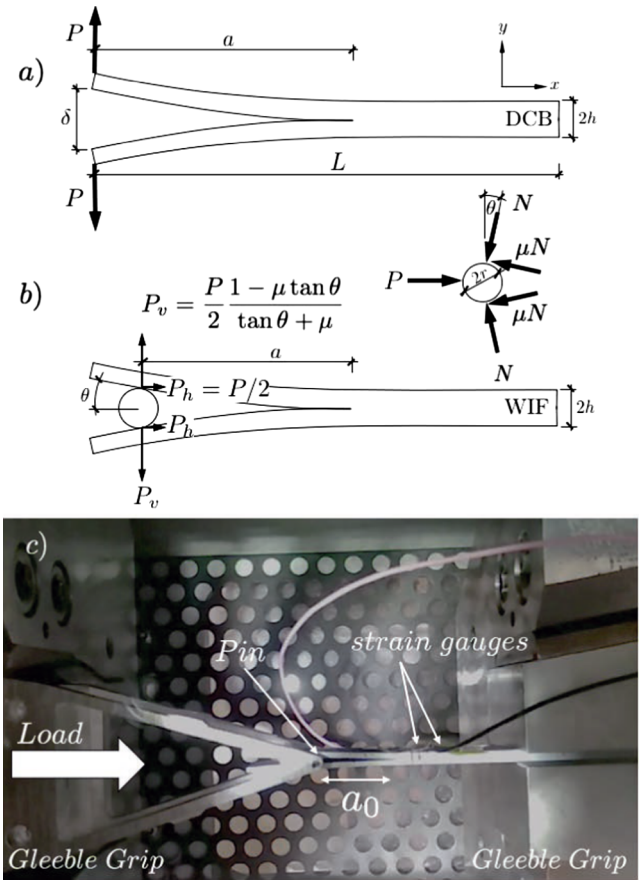

Fig. 1. Sketch of the DCB (a) and WIF (b) specimens, (c) view of the WIF specimen installed in the Gleeble 3800-GTC system. (For interpretation of the references to color in this figure legend, the reader is referred to the web version of this article.)

reduce the effect of resin rich regions at the tip of the Teflon insert. The lateral side of each specimen was sprayed with white primer paint and the 60 mm after the pre-crack marked in 1 mm increments to track crack growth throughout the test. The tests are conducted by imposing a constant DCB arm opening $\dot{\delta}$ while recording the load applied P. Quasi-static fracture test were conducted through use of $\dot{\delta} = 0.5 - 450$ mm/min as cross-head speed in an Instron 5966 screw driven universal testing frame.

For the dynamic loading conditions, the wedge-insert fracture method (WIF) was applied to avoid the introduction of asymmetric arm loads which results in mix mode loading rather than pure mode I loading. This paper follows the geometry suggested by Kusaka et al. [10] which make use of paralepipedic specimens of $L = 125$ mm, width $b = 25$ mm and thickness $2h = 3$ mm. The load P in the specimen is introduced by means of a small diameter cylinder of radius $r = 0.75$ mm as it is shown in Fig. 1(b). The cylinder is subjected to two forces, namely P_h and P_v, from the corresponding contacts with the arms while P is the load transmitted by the testing system. Assuming that the mass of the cylinder is negligible, and thus, the corresponding inertial effects, the vertical and horizontal forces can be related to the applied force P as

$$P_v = \frac{P}{2}\frac{1-\mu\tan\theta}{\tan\theta+\mu} \text{ and } P_h = \frac{P}{2} \tag{1}$$

where μ and θ stands for the friction coefficient and beam angle in Fig. 1(b), respectively. For small angle values, $\theta \to 0$, the horizontal and vertical forces are related by a Coulomb law $P_h \approx \mu P_v$, which essentially means that the in-plane compressive load transmitted to the laminate P is limited by the maximum value of P_v. Although friction may have an strong effect on the value of the WIF force P, the strategy followed in this work is based on the indirect measurement of P_v by means of the strain gauges attached to the specimen. This method circumvents the use of the load cell signal of the testing machine and the initial knowledge of the friction coefficient [29]. The effect of friction was also corroborated in this work by means of numerical simulations using the finite element model presented in Section 4.

WIF tests were carried out using a Gleeble 3800-GTC thermal-mechanical physical system. It is based on a closed-loop hydraulic servo system which provides a precise control of both the load and displacement. The system is able to provide maximum stroke up to $\dot{\delta} = 2000$ mm/s. Two strain gauges of $350 \pm 0.3\%$ Ω and 3 mm in length were attached to the bending surface of the WIF specimen at 15 mm and 30 mm from to the initial crack tip. The effective measuring length of the strain gauges was ≈ 3 mm. A data acquisition system QuantumX MA-840A was used for recording strain gauge signals at a frequency of 2 kHz. Such strain signal was used to estimate the cantilever opening force, P_v, and thus, the interlaminar toughness of the materials, G_{Ic} as it will be shown subsequently. A thin ≈ 1.5 mm rubber nitrile sheet was used for gripping the specimens and the loading pin to the Gleeble system to avoid the transfer of parasitic oscillations from/to the specimen. The specimens were stored in dry conditions prior to the test that were carried out under room temperature. The fracture surfaces of the tested coupons were examined by scanning electron microscopy (EVO MA15, Zeiss using 15 kV potential and a vacuum pressure between 10 and 15 Pa) to ascertain the dominant fracture mechanisms. Details of the fracture mechanisms were also determined using X-ray computed tomography (Nanotom 160NF from General Electric-Phoenix). Tomograms were collected at 90 kV and 100 μA using the tungsten target. For each tomogram, 2000 radiographs were acquired with an exposure time of 750 ms. Tomogram voxel size was set approximately to 10 μm/voxel. XCT was carried out with the WIF pin inserted between the beam arms of the specimen after testing to visualize the fracture mechanisms inside the opened crack.

2.2. Data reduction method for fracture analysis

Assuming the postulates of linear elastic fracture mechanics (LEFM), the energy release rate G_{Ic} may be obtained from the variations of the elastic energy of the system when a crack extension Δa is produced. For bidimensional solids of width b, the energy release rate can be expressed as

$$G_{Ic} = \frac{P_c^2}{2b}\frac{dC}{da} \tag{2}$$

where P_c is the critical applied load and $C(a)$ the elastic compliance of the system. It should be remarked that this expression is valid if the kinetic energy is small compared with the strain energy. In the case of a double-cantilever beam (DCB) subjected to a pair of self-equilibrated forces P, and with an opening displacement of the arms δ, the experimental compliance for a given crack length $C(a) = \delta/P$ can be fitted to the following mathematical expression as suggested by Hojo et al. [28]:

$$\frac{a}{2h} = \alpha\sqrt[3]{bC} + \beta \tag{3}$$

where α and β are the corresponding fitting parameters. Upon substitution of Eq. (3) into (2), a simple expression for the interlaminar toughness of a DCB specimen can be obtained

$$G_{Ic}^{DCB} = \frac{3}{4h}\left(\frac{P_c}{b}\right)^2\frac{\sqrt[3]{(bC(a_c))^2}}{\alpha} \tag{4}$$

where P_c is the critical load at the onset of crack extension and a_c the crack length in this situation. In addition, assuming that the DCB arms behave as elastic cantilever beams, the relation between the total arm opening displacement δ and the maximum strain at the fixed end ϵ is given by

$$\epsilon = \frac{3}{4}\frac{h}{a^2}\delta \tag{5}$$

where ϵ can be understood as the nominal strain representative of some local loading conditions near the crack tip. The ratio between the cross-head displacement rate $\dot{\delta}$ and the nominal strain-rate prior to the onset of fracture is given in this case by the following mathematical expression

$$\dot{\epsilon} = \frac{3}{4}\frac{h}{a^2}\dot{\delta} \tag{6}$$

In this case, it is assumed that no growth is produced. For WIF specimens, if the contact angle θ is sufficiently small, of a few degrees, the term corresponding to the horizontal forces can be neglected which gives an expression similar to the DCB presented in Eq. (2). As it has been mentioned previously, strain gauges were installed in the bending surface of the specimens at given distances, 15 mm and 30 mm, from the initial crack tip in order to estimate the opening force P. By using the small deflection theory, the strain ϵ detected by one of these gauges when the crack is located in the same beam section is given by

$$\epsilon = \frac{P_v a}{E_1 I}\frac{h}{2} \tag{7}$$

where I stands for the inertia moment of the rectangular cross-section of the arm ($I = 1/12bh^3$), and E_1 is the longitudinal modulus of the laminate. Similarly, an indirect compliance term D, relating the strain gauge reading ϵ with the applied force P can be obtained by

$$\frac{\epsilon}{P_v} = \frac{ha}{2E_1 I} = D(a) \tag{8}$$

This latter term can be understood as an indirect compliance factor $D(a)$ relating the applied load and the strain gauge signal. This compliance term can be estimated from the beam theory as in the previous Eq. (8), by means of finite element simulations or by measuring it in dedicated experiments with instrumented DCB specimens. For an arbitrary crack length a, the indirect compliance term can be estimated from (8) as $D(a) = D(a_0)a/a_0$ where a_0 stands for a reference or initial crack length. Finally, the critical arm loading for WIF configurations can be determined as

$$P_{vc} = \frac{a_0}{D(a_0)}\frac{\epsilon_c}{a_c} = \frac{a_0}{D(a_0)}\frac{\epsilon_c}{2h(\alpha\sqrt[3]{b\frac{2r}{P_{vc}}} + \beta)} \tag{9}$$

where $D(a_0)$ is the indirect compliance term for the reference crack length a_0, and a_c and ϵ_c stand for the crack length and strain at the onset of fracture, respectively. The crack length a_c can be determined from the specimen compliance $C(a_c) = 2r/P_{vc}$ using expression (3). After determination of the critical load P_{vc} from the strain gauge reading ϵ_c, the fracture toughness of the WIF specimen is computed as

$$G_{Ic}^{WIF} = \frac{3}{4h}\left(\frac{P_{vc}}{b}\right)^2\frac{\sqrt[3]{(bC(a_c))^2}}{\alpha} \tag{10}$$

In this second case, the arm opening corresponded to the diameter of the loading pin $2r$. Therefore, the beam deflection can be expressed as a function of the strain gauge reading as:

$$r = \frac{2}{3}\frac{a^2}{h}\epsilon \tag{11}$$

By taking the time differential of the previous expression with $\dot{r} = 0$ and assuming that if the crack does not grow, the distance a between the loading pin and the crack tip decreases at the same rate as the WIF displacement is produced ($\dot{a} = -\dot{\delta}$). Therefore, the strain gauge rate can be computed as:

$$\dot{\epsilon} = \frac{2\epsilon}{a}\dot{\delta} \tag{12}$$

where $\dot{\delta}$ stands for the WIF displacement rate applied. However, it should be mentioned that in the latter expression, the exact distance between the pin and the crack tip at the onset of fracture is unknown so it is somewhat difficult to determine the strain-rate from the WIF displacement rate. In this case, a direct measurement using the strain gauges attached to the surface of the sample is preferred. Similar analysis as described in the previous paragraphs can be made to determine the angle θ, see Fig. 1(b), at the onset of fracture which is given by $\theta = a\,\epsilon_c/h$.

Table 1
Elastic moduli of the IM7/8552 (upper) and IM7/M91 (lower) for different strain-rates.

Property	$\dot{\epsilon} = 4\times10^{-4}\,s^{-1}$	$\dot{\epsilon} = 4\times10^{-3}\,s^{-1}$	$\dot{\epsilon} = 4\times10^{-2}\,s^{-1}$
E_1 (GPa)	168.1 ± 3.3	165.7 ± 6.8	171.6 ± 1.4
	163.2 ± 5.9	169.8 ± 6.6	165.2 ± 1.8
E_2 (GPa)	8.5 ± 0.2	8.6 ± 0.4	9.9 ± 0.1
	7.8 ± 0.2	8.1 ± 0.2	9.6 ± 0.2
G_{12} (GPa)	6.1 ± 0.1	5.4 ± 0.1	6.2 ± 0.1
	5.2 ± 0.3	5.2 ± 0.2	5.8 ± 0.2

3. Results

3.1. Tensile and calibration tests

Five tensile tests at different cross-head speeds between $\dot{\delta} = 0.5$ and 450 mm/min were conducted on the $[0°]_4$, $[90°]_8$ and $[\pm45°]_{4s}$ specimens in order to determine experimentally the E_1, E_2 and G_{12} moduli, and their strain-rate dependence in this range of $\dot{\delta}$. The strain-rate, $\dot{\epsilon}$, was determined from the time evolution of the strain in the loading direction which was recorded by means of the video extensometer. The results are gathered in Table 1, including the average values and the standard deviation corresponding to five valid tests. Not surprisingly, the results of elastic moduli did not exhibit strain-rate dependence, at least, in the range of velocities analyzed.

Quasi-static fracture tests were carried out using IM7/8552 and IM7/M91 DCB specimens using a range of cross-head speeds between $\dot{\delta} = 0.5$ and 450 mm/min. Fig. 2 shows the representative load-displacement curves corresponding to both materials at the minimum $\dot{\delta} = 0.5$ mm/min and maximum $\dot{\delta} = 450$ mm/min cross-head speeds. The general shape of the load-displacement curve was similar in all the cases and showed stable and smooth crack propagation independent of the cross-head speed imposed. A first look at the $P-\delta$ curves shows that the interlaminar toughness of the IM7/M91 specimens was higher than the IM7/8552, and that the corresponding values of the toughness decreased in both materials between as $\dot{\delta}$ was increased.

The load-displacement curves were used to determine the compliance $C(a) = \delta/P$ which is plotted in Fig. 3. The compliance of the specimen required for fracture test data reduction is essentially dominated by the rate independent elastic behaviour of the arm material in the fiber direction. The parameters α and β from Eq. (3) were determined by least-squares fitting through using all the values of the compliance measured irrespective of the cross-head speed applied. The results are gathered in Table 2.

Some DCB specimens were used to calibrate the indirect compliance $D(a) = \epsilon/P$ term necessary to estimate the critical load from the measurement of the strain near the crack tip area in the WIF specimens, Eq. (8). To this end, standard DCB specimens with $a_0 = 30$ mm as reference crack length were instrumented with a strain gauge installed just at the position of the initial crack tip. The displacement rate used for the calibration ranged from $\dot{\delta} = 0.5$ to 450 mm/min with the load P and the strain ϵ recorded to determine the value of $D(a_0)$ in all the cases. The results obtained for both materials are gathered in Fig. 4(a). As in the previous cases, the indirect compliance D did not exhibit significant strain-rate dependence in the displacement range analyzed, as bending is essentially dominated by the carbon fiber behaviour which is strain-rate insensitive. In addition, the estimation of $D(a_0)$ based on Eq. (8)

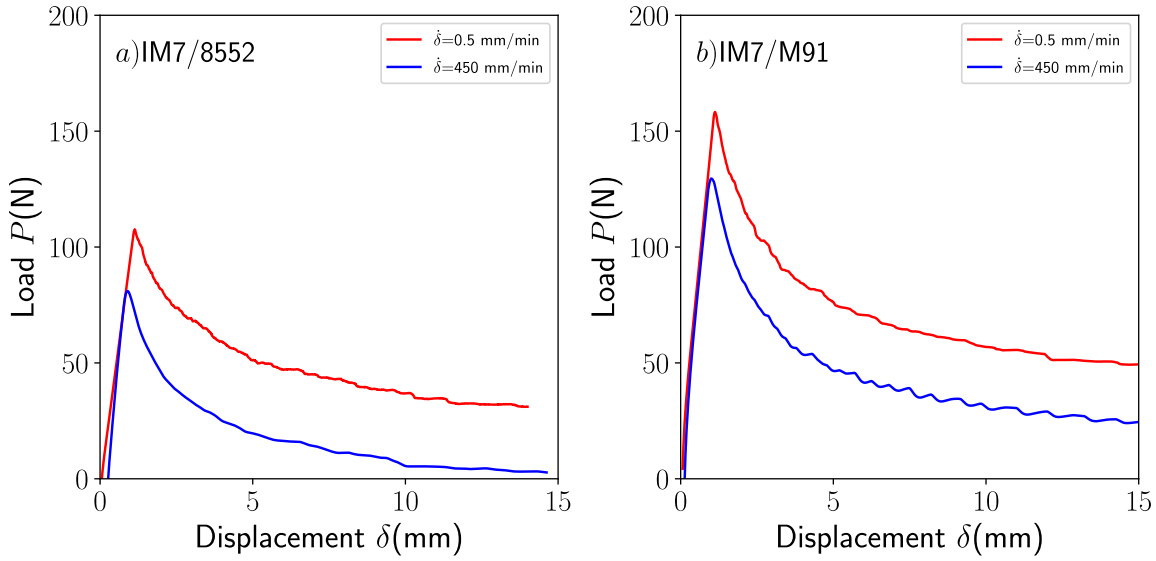

Fig. 2. Experimental $P-\delta$ curves for applied displacement rates $\dot{\delta}$ of 0.5 mm/min and 450 mm/min in DCB specimens: (a) IM7/8552, (b) IM7/M91. (For interpretation of the references to color in this figure legend, the reader is referred to the web version of this article.)

using the elastic constants presented in Table 1 is plotted as a red transparent rectangle in Fig. 4(a) for a direct comparison. The final values of $D(a_0)$ used for data WIF data reduction are presented in Table 2. The corresponding values for an arbitrary crack length a were obtained assuming $D(a) = D(a_0)a/a_0$ as was previously described.

3.2. Fracture toughness results

Once calibration experiments were performed, an experimental campaign of fracture tests using quasi-static DCB and dynamic WIF specimens was carried out. The campaign included at least five valid tested specimens loaded under different strain-rates using DCB ($\dot{\delta}$ = 0.5, 4.5, 45, 450 mm/min) and WIF ($\dot{\delta}$ = 100, 500, 1000, 2000 mm/s) configurations. It was assumed that calibration parameters measured under quasi-static conditions can be used under dynamic conditions under the assumption that both $C(a)$ and D are controlled by the bending behaviour of the unidirectional composites which is assumed to be strain-rate insensitive.

Table 2
Calibration parameters for fracture toughness data reduction. Parameters α and β, see Eq. (3) and D see Eq. (8) using a reference crack length a_0 = 30 mm.

Value	IM7/8552	IM7/M91
α ($N^{-1}\,mm^{2/3}$)	11.42	11.69
β(.)	0.151	−0.197
D (N^{-1})	$2.225\cdot10^{-5}$	$1.937\cdot10^{-5}$

DCB quasi-static results obtained for IM7/M91 and IM7/8552 are gathered together in Fig. 4(b), including the average values and the standard deviation of the five valid tests. In both materials, delamination toughness was slightly higher when testing at very low displacement rates. Such an effect could probably be attributed to some viscous stress relaxation mechanisms occurring at the crack tip. IM7/8552 interlaminar quasi-static toughness values were in same range as reporter by other authors [30]. WIF fracture tests were carried out in the Gleeble

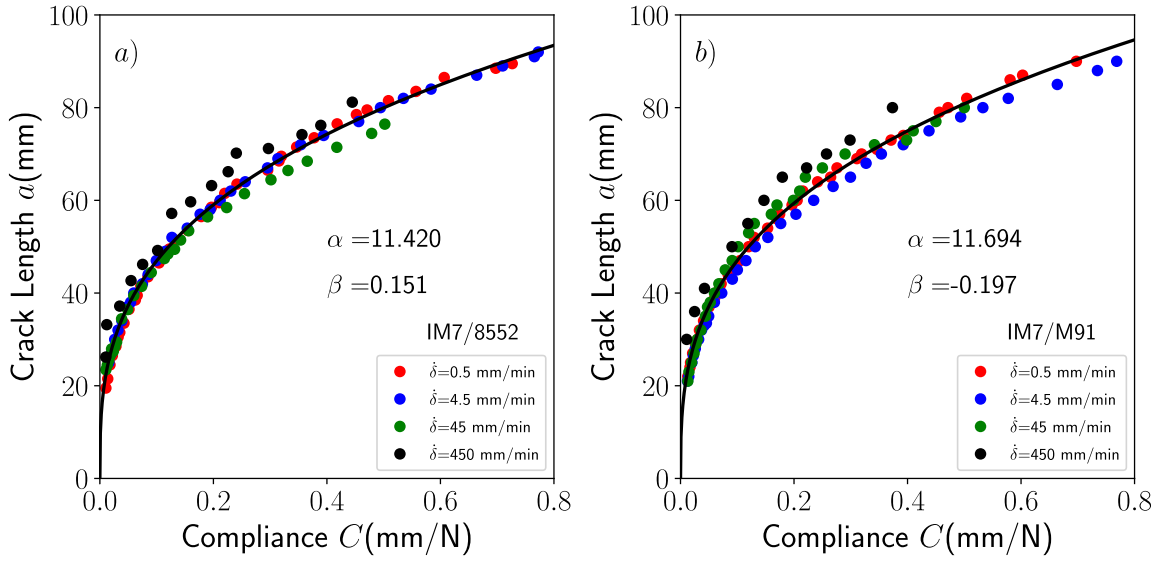

Fig. 3. Experimental measurements of DCB crack length a and compliance $C(a)$ at different displacement rates: (a) IM7/8552, (b) IM7/M91. The results also include the best least-square fitting using Eq. (3) in a black continuous line. (For interpretation of the references to color in this figure legend, the reader is referred to the web version of this article.)

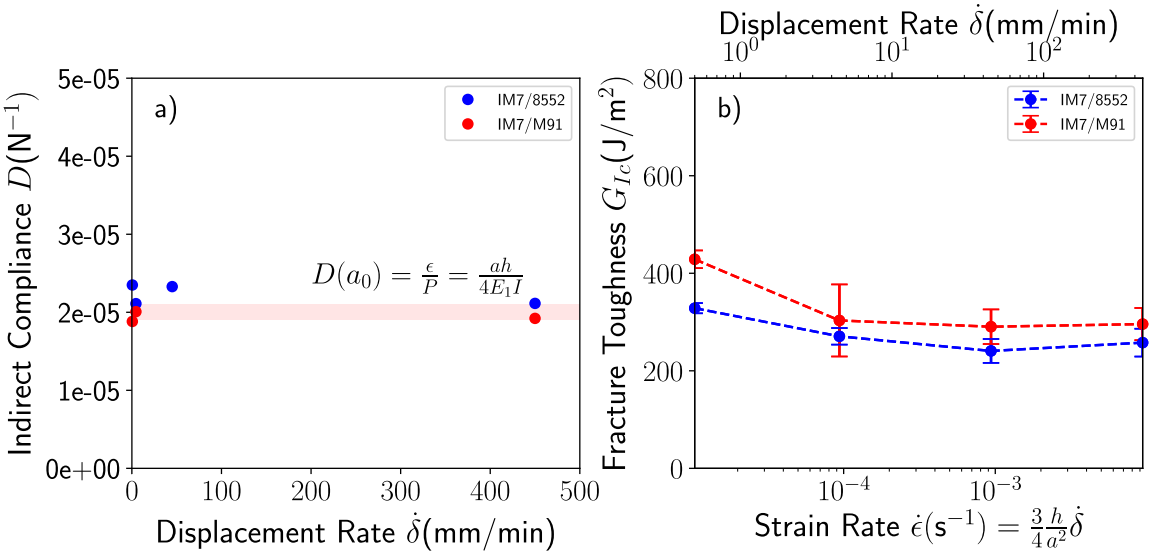

Fig. 4. (a) Experimental measurements and theoretical values of the calibration factor $D(a_0) = \epsilon/P$ for IM7/8552 and IM7/M91 laminates using a nominal crack length of $a_0 = 30$ mm, (b) strain rate dependence of interlaminar fracture toughness G_{Ic} for IM7/8552 and IM7/M91 laminates obtained using quasi-static DCB tests. The strain rate indicator used was determined from the beam theory in Eq. (6) as $\dot{\epsilon} = \frac{3}{4}\frac{h}{a^2}\dot{\delta}$ where $\dot{\delta}$ is the DCB displacement rate. (For interpretation of the references to color in this figure legend, the reader is referred to the web version of this article.)

3800-GTC system. Two strain gauges were installed at ≈ 15 mm and ≈ 30 mm ahead of the initial crack tip. The strain gauge readings, ϵ_1 and ϵ_2 respectively, were presented for IM7/8552 and IM7/M91 laminates tested at $\dot{\delta} = 100$, 500 and 2000 mm/s in Fig. 5 and Fig. 6. The signal of the strain gauges was first smoothed using a Savitzky-Golay filter [31] with third order polynomials and fifty-one data points as window size, providing a more precise time-derivative for the strain-rate determination. Variations of the filter parameters, polynomial degree and window size provided similar results of the strain-rate within the experimental scatter. The strain ϵ_1 and ϵ_2 rose suddenly as a consequence of the dynamic loading reaching a peak which was attributed to the pass of the moving crack front through the section where the strain gauges were installed. An estimation of the crack propagation velocity can be obtained from the temporal shift between the strain peaks Δt, see Fig. 5(a), and the separation between the installed strain gauges $\Delta l \approx 15$ mm. For the three test cases presented in Fig. 5, the propagation speeds were 2600, 470 and 160 mm/s for the nominal speeds of 2000, 500 and 100 mm/s imposed by the Gleeble testing machine. The discrepancies were endorsed to errors in the distance between strain gauges during the attachment process.

The maximum value of the strain-rate obtained by numerical derivative was determined for all the tests corresponding to an intermediate position between the initial rise from the strain signal, and its maximum value ϵ_c. The average values and standard deviation of the maximum strain-rate obtained from the signals ϵ_1 and ϵ_2 were plotted for the different displacement rates in Fig. 7(a). In both materials, the relation between the strain-rate and the pin displacement rate was linear within the experimental scatter, although the slope was slightly different in both cases and greater in the IM7/M91 material than IM7/8552.

The value of the strain gauge reading at the peak ϵ_c, obtained for both materials at different displacement rates, was used to estimate the arm load and the fracture toughness under dynamic conditions by means of the expression previously described (10). The corresponding plots of the interlaminar fracture toughness as a function of the strain-rate including all the results obtained with DCB and WIF specimens are presented in Fig. 7(b). As in the quasi-static test, IM7/M91 was tougher than IM7/8552. Therefore, for the same nominal geometry, the corresponding critical strain ϵ_c at the onset of crack propagation is considerably higher (see Fig. 5 and Fig. 6). The interlaminar fracture toughness of the IM7/8552 material followed the same trends observed in the quasi-static tests with average values in the order of 300 J/m^2. However, IM7/M91 toughness presented a continuous increase up to the maximum value of 577 ± 50 J/m^2 for $\dot{\delta} = 500$ mm/s which is almost the double that shown under quasi-static conditions ($\dot{\epsilon} = 0.36\ s^{-1}$). This increase in the interlaminar toughness of the IM7/M91 was not detected in the IM7/8552 one. Remarkably, the peak of toughness observed for IM7/M91 laminates did not occur for the maximum displacement rate but an intermediate one. Even in this case, the toughness obtained for $\dot{\delta} = 2000$ mm/s was 440 ± 33 J/m^2 which is ≈ 50% higher than the quasi-static value.

3.3. Fracture mechanisms

The fracture surfaces of the tested DCB and WIF specimens were first visualized using a scanning electron microscope. The results are gathered in Fig. 8 for both materials, and three displacement rates of $\dot{\delta} = 0.5$, 500 and 2000 mm/s. In the case of the IM7/8552 material, the fracture surface was totally flat irrespective of the displacement rate with some evidence of fiber/matrix interface fracture and fiber bridging, Fig. 8(a) and (b). However, the appearance of the fracture surfaces of the IM7/M91 laminates was totally different. In this case, the fracture surface included some strips following the fiber direction, providing evidence of ductile fracture propagating through the interleave material while the remaining surfaces were very similar to those observed in the IM7/8552. This pattern of intercalated regions, Fig. 8(c) and (d), was only observed in the IM7/M91 laminate. The relative area of the ductile strips to the total fractured area, namely f, for the IM7/M91 laminate was determined using image analysis with the SEM micrographs. The results are gathered in Fig. 7(b). Not surprisingly, this relative area followed the same trends as detected in the fracture toughness of the IM7/M91 laminate, suggesting that the strain-rate sensitivity could be attributed to changes in the crack patterns rather than an intrinsic dependence. A crude comparison can be carried out by assuming that the fracture energy of the IM7/M91 interleaved laminate is $G_{pred} = fG_{sup} + (1 - f)G_{inf}$ with $G_{inf} = 300$ J/m^2 and $G_{sup} = 700$ J/m^2. These values could be representative of brittle and ductile fracture toughnesses. The results are presented in Fig. 7(b) and the comparison is reasonable for the whole displacement rate analyzed. The most plausible fracture mechanism could be attributed to crack migration from the interleaved region into the fiber ply. It is highly likely that the

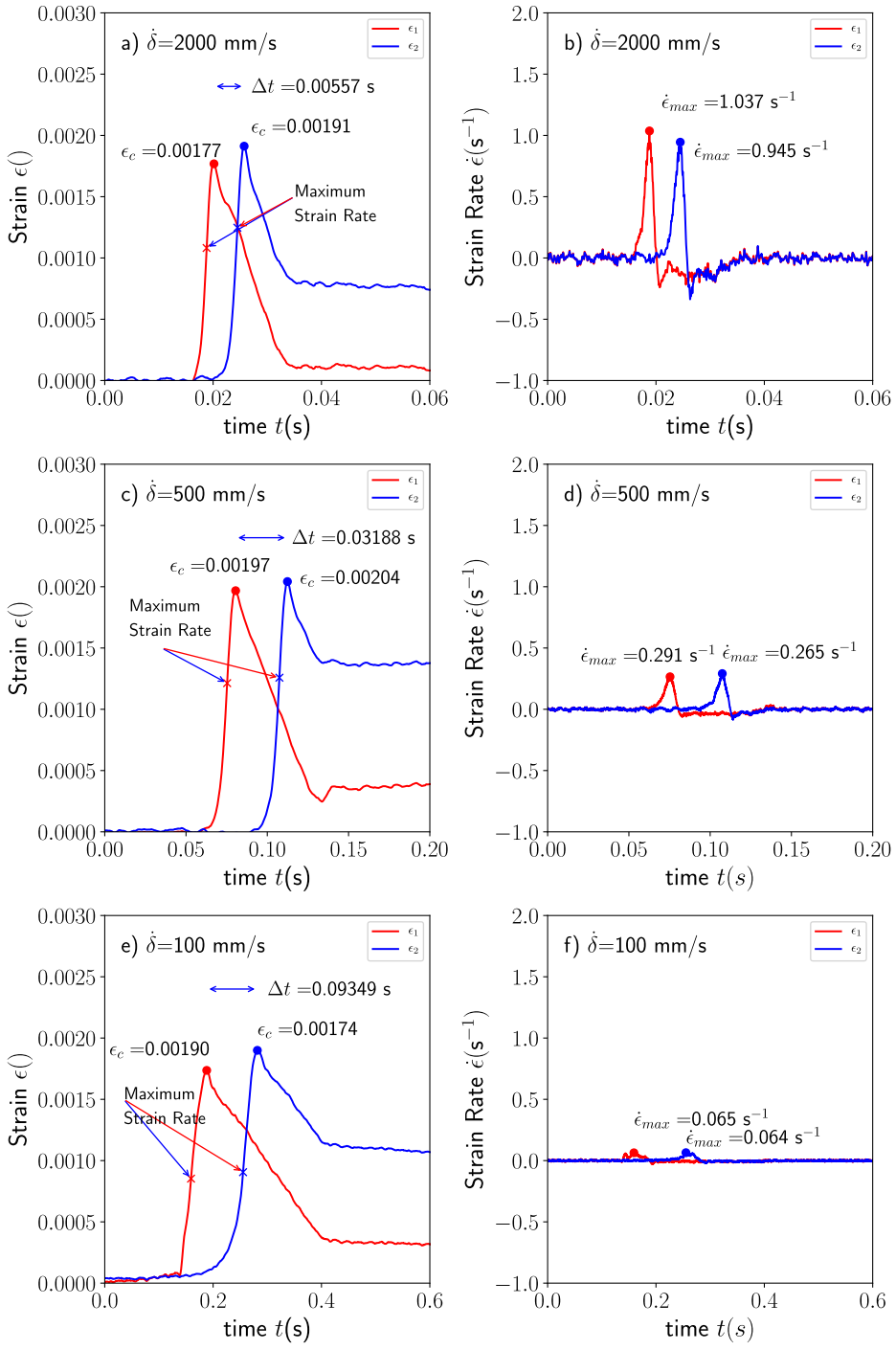

Fig. 5. Strain and strain-rate evolution curves corresponding to two strain gauges attached at 15 mm (ϵ_1) and 30 mm (ϵ_2) from the initial crack tip in a IM7/8552 specimens tested at $\dot{\delta}$ = 2000 mm/s, $\dot{\delta}$ = 500 mm/s and $\dot{\delta}$ = 100 mm/s displacement rates. Strain-rates were numerically determined from the gauge readings filtered using a Savitzky-Golay filter. (For interpretation of the references to color in this figure legend, the reader is referred to the web version of this article.)

presence of particles enhanced the dynamic behaviour of the resin in the interleaved region. Thus, ductile tearing was triggered by particle interface debonding. At some point, the crack deflects and kinks into the fiber ply, producing a set of highly active fiber bridges. However, it is still unclear why this mechanism presents an absolute maximum in the fracture toughness at $\dot{\delta}$ = 500 mm/s.

X-ray tomograms were acquired to clarify the previously described fracture mechanisms. Fig. 9(a) and (b) shows two cross-section of IM7/M91 tested laminates in the fiber direction for the material tested at $\dot{\delta}$ = 500 mm/s. The first one, Fig. 9(a), shows evidences of crack propagation through the interleave. The presence of the particles shields the stress field in the crack tip, with the crack tending to propagate and then link previously previously debonded neighbor particles. In addition, the second one, see Fig. 9(c), shows the cross-section of the laminate perpendicular to the crack direction where there is evidence of the formation of the aforementioned ductile strips. This forms bridges that span the crack faces and contribute to the enhancement of the fracture toughness detected in the experiments.

4. Modelling

The dynamic fracture of the WIF specimens presented in the

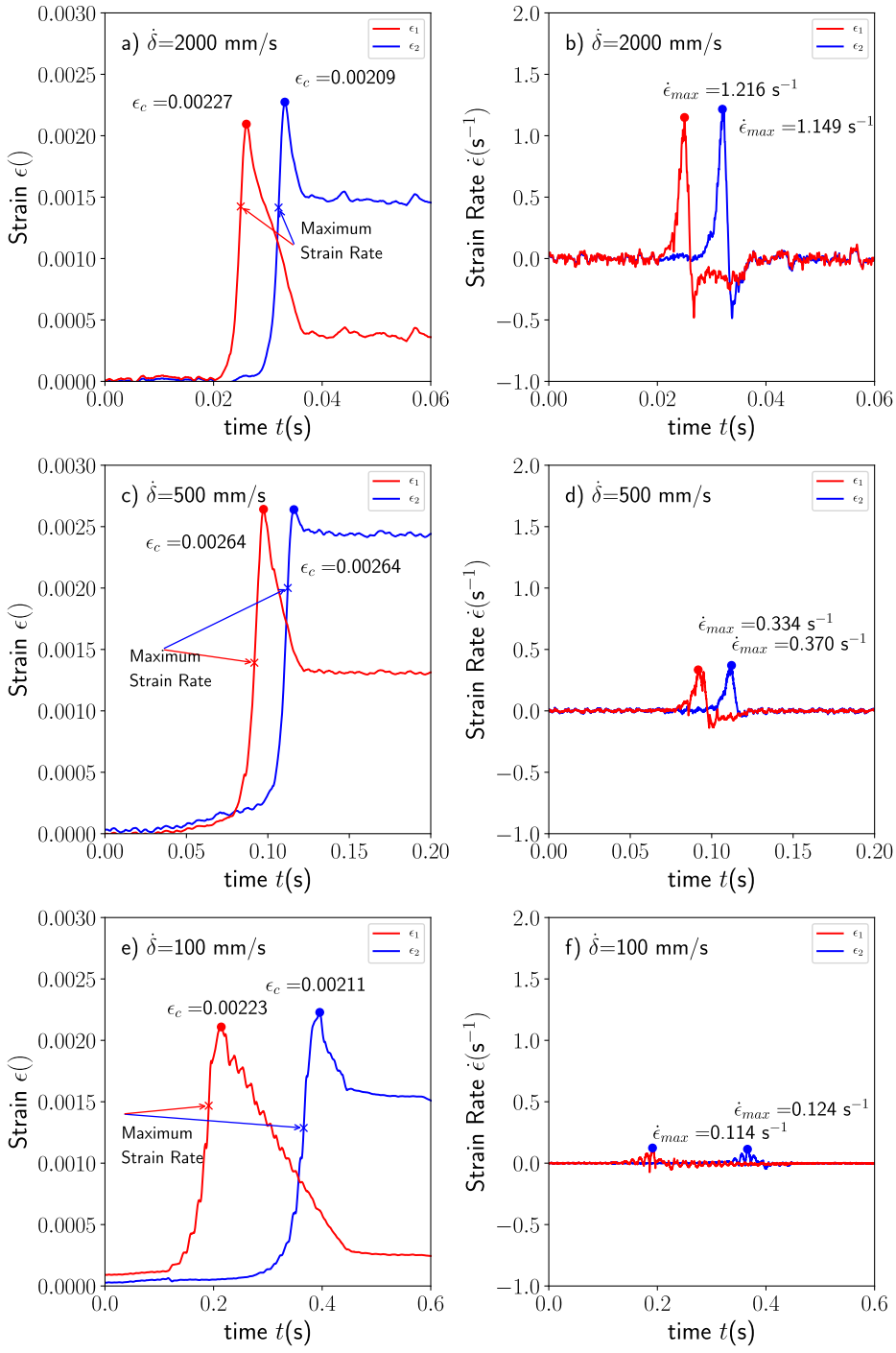

Fig. 6. Strain and strain-rate evolution curves corresponding to two strain gauges attached at 15 mm (ϵ_1) and 30 mm (ϵ_2) from the initial crack tip in a IM7/M91 specimens tested at $\dot{\delta}$ = 2000 mm/s, $\dot{\delta}$ = 500 mm/s and $\dot{\delta}$ = 100 mm/s displacement rates. Strain-rates were numerically determined from the gauge readings filtered using a Savitzky-Golay filter. (For interpretation of the references to color in this figure legend, the reader is referred to the web version of this article.)

previous sections was simulated using a 2D finite element model in the plane $x - y$. The geometry corresponded to the dimensions presented in Fig. 1 with length and thickness of $L = 125$ mm and $h = 3$ mm, respectively, and by assuming unit width of specimen under plane strain conditions. Both halves of the WIF specimen were modeled individually and discretized through using 2D reduced integration plane strain elements in Abaqus (CPE4R). The arms of the WIF specimen were assumed to behave as anisotropic solids with the fiber direction in the direction of the specimen length. The elastic properties of the unidirectional material used in the simulation are shown in Table 1. The mesh close to the crack tip was refined to account for the stress gradients in the fracture process zone. Fracture propagation was simulated using the cohesive zone model (CZM). A layer of cohesive elements (COH2D4) was inserted between the WIF specimen arms. The initial response of the cohesive elements was linear and elastic in the absence of damage with the traction-separation law given by $t_n = K\Delta_n$ and $t_t = K\Delta_t$, where t_n, t_t, Δ_n and Δ_t stand for the normal and shear tractions and the displacement jumps across the interface, respectively. The elastic stiffness was set to $K = 10^5$ MPa/mm to ensure displacement continuity across the specimen arms in the absence of damage. The onset of damage in the cohesive elements was dictated by the maximum stress criterion as

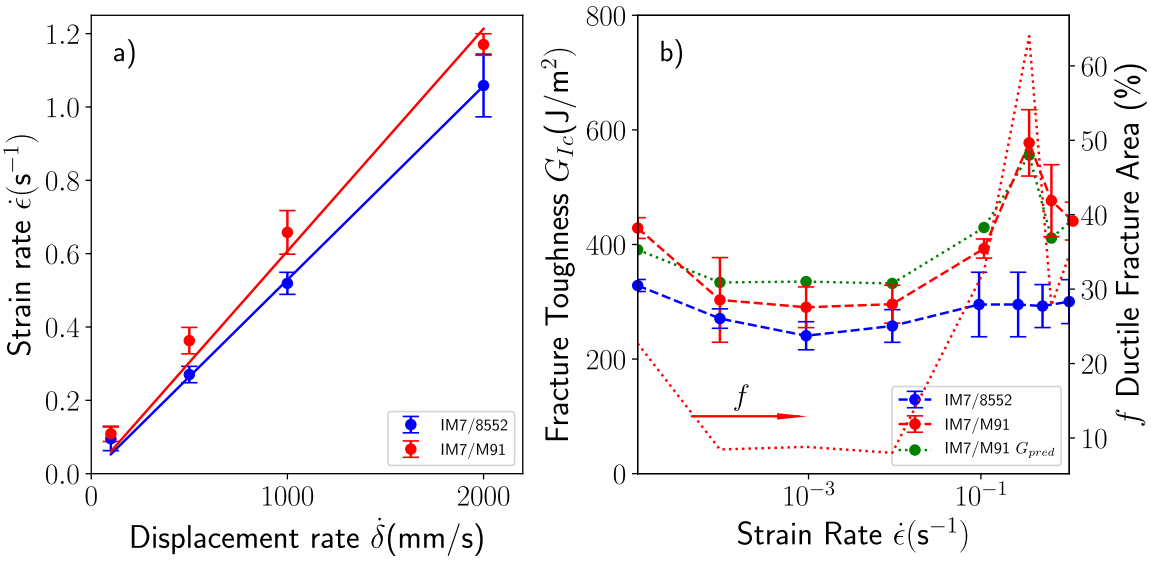

Fig. 7. (a) Relation between gauge strain-rate and displacement rate in WIF specimens, (b) strain-rate dependence of interlaminar fracture toughness G_{Ic} for IM7/8552 and IM7/M91 laminates obtained using DCB and WIF specimens. The ratio of ductile fracture surface to total fracture surface f for the IM7/M91 material is also presented in a second vertical axis. (For interpretation of the references to color in this figure legend, the reader is referred to the web version of this article.)

$$(\frac{<t_n>^2}{N})^2 + (\frac{<t_s>^2}{S})^2 = 1 \tag{13}$$

where N and S represent the normal and shear strength of the cohesive elements and $<>$ the Macaulay operator defined as $<x> = (x + |x|)/2$. After the onset of damage, crack propagation is controlled by a linear softening law, using the damage variable d, so the stress transfer is now defined as $t_n = (1 - d)K\Delta_n$ and $t_t = (1 - d)K\Delta_t$ ($d = 0$ in the absence of damage and $d = 1$ for a fully damaged cohesive element). The area associated with the cohesive law is given by the interface fracture energy in mode I and II (G_{Ic} and G_{IIc}). Mode I is expected since the loading is symmetric. Shear strength and mode II fracture toughness are secondary and their values were assumed to be equal to the normal strength and mode I toughness. The length of the cohesive elements used was 0.25 mm to ensure a good reproduction of the stress fields in the fracture process zone. No strain-rate effects were introduced in the cohesive properties formulation. By assuming the linear softening law controlling the $t_n - \Delta_n$ relationship, the normal separation of the cohesive elements corresponding to the onset of fracture is given by $\Delta_{n0} = N/K$ while the corresponding value for the total separation is $\Delta_{nc} = 2G_{Ic}/N$.

Simulations were run in two subsequent steps. First, the cylinder insertion between the arms was simulated by opening them gradually with two semi-cylinders moving in an opposite vertical y direction without displacements in the mid-plane of the laminate. Contact surfaces with frictionless behaviour were introduced between the arm and the corresponding curved surface of the semi-cylinders. The insertion step ends when the two horizontal diameters of the semi-cylinders reach the same position. This step was followed by a rigid body translation of the semi-cylinders along the length of the specimen at a given rate of $\dot{\delta}$. Simulations were carried out using implicit dynamic integration within Abaqus Standard v2016 under the large displacement framework. For problems involving contacting surfaces, the Hilber-Hugues-Taylor operator was used with $\alpha = -0.41421$, $\beta = 0.5$ and $\gamma = 0.91421$ parameters as suggested by the software. After the wedge was inserted between specimen arms, a fixed displacement of 80 mm was imposed along the x direction. The simulation was stopped then and the history results, corresponding to the arm loading and average strain of the two strain gauge areas, were recorded for the analysis. The strain obtained from the simulation corresponded to the average values of all the elements within the strain gauge regions which were 3 mm in length.

4.1. Validation of the data reduction method and correlation with experiments

Firstly, the FEM model described above was used to check the accuracy of the data reduction method for WIF specimens as previously described. To this end, a set of simulations was carried out using WIF displacement rates ranging from $\dot{\delta} = 100$ to 2000 mm/s and fracture toughness of the cohesive elements between $G_{Ic} = 300$ and 700 J/m^2. The tensile strength of the cohesive elements was set to $N = 50$ MPa in all the cases. This is a typical value of the transverse strength of a unidirectional ply. The average gauge strains, ϵ_1 and ϵ_2 obtained from the model, were used to determine the dynamic fracture toughness as was done with the experimental results. Fig. 10(a) gathers the results obtained with the FEM model using, as inputs, the corresponding displacement rate $\dot{\delta}$ and fracture toughness G_{Ic}, while collecting after the simulation the corresponding values of the fracture toughness using the same data reduction method. This was done by taking the maximum values of the strain gauges ϵ_1 and ϵ_2 into the expression (10). The results showed the ability and accuracy of the data reduction method for the determination of the fracture toughness using the WIF specimens instrumented with strain gauges. The maximum difference between the ground true value of the toughness introduced in the FEM model and the corresponding value determined by postprocessing through use of the computed strain gauge readings is less than 10% for all the displacement rates, Fig. 10(a). In all the cases analyzed, the kinetic energy of the system was small as compared with the strain energy. Thus, inertial effects can be neglected.

The evolution of the crack length was determined using the results obtained from the finite element simulations. The crack tip was automatically detected through use of a Python script in Abaqus using the point of the mid-plane of the laminate where the cohesive stresses reached the maximum value equal to N. The results obtained are summarized in Fig. 10(b) for the four WIF displacement rates analyzed and the two bounding fracture energies used. The shape of each curve is the same regardless of the parameters used in the model. There is a first, pre-critical, part of the curve where the crack length evolves slowly until the condition of a fully damaged cohesive element is fulfilled (the normal separation of the cohesive elements reached $\Delta_{nc} = 2G_{Ic}/N$). After this point, the cohesive crack is translated along the mid-plane of the laminate in a self-similar way. The slope of the curves in this second region corresponded to the WIF displacement rate imposed $\dot{\delta}$. It is

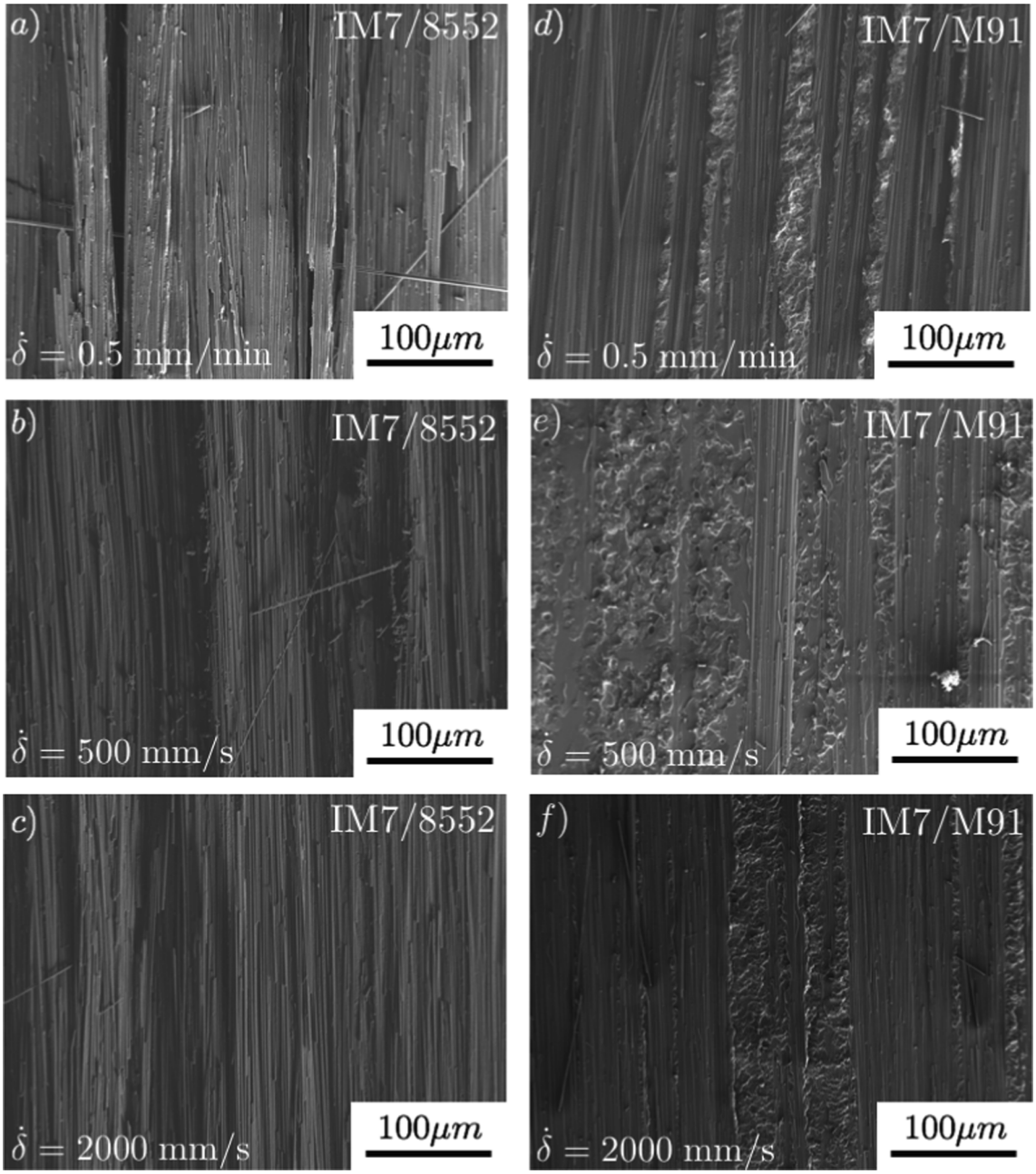

Fig. 8. Fracture surface of the DCB and WIF specimens of IM7/8552 and IM7/M91 laminates at different displacement rates. Evidences of ductile tearing in the interleave for IM7/M91 material can be observed in micrographs (d), (e) and (f). The ratio of the ductile fracture surface to the total fracture surface *f* for IM7/M91 was determined by image analysis and the results presented in Fig. 7(b) as compliment.ary information. (For interpretation of the references to color in this figure legend, the reader is referred to the web version of this article.)

important to note that the position of the strain gauges for fracture property measurement should be far enough away from the crack tip to avoid any transient phenomena prior to the constant velocity propagation of the crack.

Secondly, a set of new simulations was carried out for IM7/8552 and IM7/M91 using the experimental fracture toughness of the WIF specimens presented previously (see Fig. 7). The comparison of the strain gauge readings obtained in the simulation and the experimental ones are gathered in Fig. 11. It should be mentioned that the temporal scale of the experimental signal was first shifted to match the rise of both experimental and numerical signals ϵ_1. The discrepancies between the temporal position of the second signal ϵ_2 in some of the cases, as is shown in Fig. 11(c), may be attributed to positional mistakes made during the installation and attachment of the strain gauges which were nominally separated by 15 mm. However, in all the cases computed, both the maximum amplitude and the shape of the decay after the onset of fracture were reasonably captured by the simulations. A new set of simulations was run using different pin/composite friction coefficients of $\mu = 0$, 0.25 and 0.50 for the IM7/M91 loaded at 2000 mm/s. The results, inserted in Fig. 11(d), practically superimposed to the curves obtained with the frictionless contact which is indicative of the appropriateness of the method to estimate the opening arm forces P_v indirectly from the strain gauge signals.

The finite element model was employed to ascertain the appropriateness of the data reduction method used in the WIF fracture tests as shown in the previous section. However, as no rate effects were introduced in the traction separation law of the cohesive elements, extrapolation to other configurations and/or velocities could be extremely

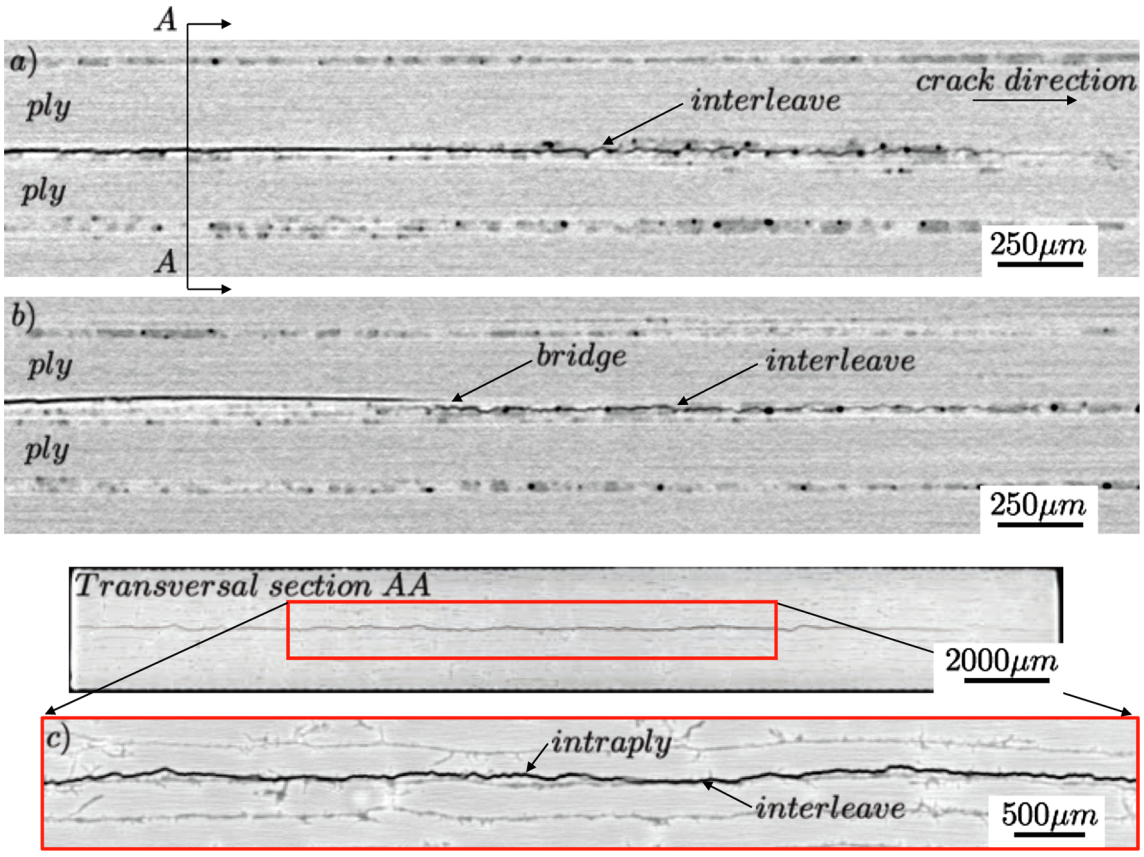

Fig. 9. X-ray tomograms of a IM7/M91 WIF laminate tested at $\dot{\delta} = 500$ mm/s: (a) and (b) represents longitudinal sections in the crack direction showing propagation through the interleaves. Images were acquired with a resolution 11.7 μm, (c) transversal sections perpendicular specimen length showing crack propagation through the interleaves and crack migration to the adjacent plies. Images were acquired with a resolution 3 μm. (For interpretation of the references to color in this figure legend, the reader is referred to the web version of this article.)

difficult if only the strain-rate is measured from the gauges installed in the specimens, see for instance Fig. 5 and Fig. 6. The time-response of the strain gauges installed could be understood as a reasonable indicator of the strain and strain-rate levels attained in the vicinity of the crack tip, but not as a detailed parameter measuring the loading rate of the crack by itself. In this respect, a finite element model can be used to infer the rates of the normal separation of the cohesive elements Δ_n, relating it to the macroscopic displacement rates imposed on the specimen.

The time-evolution of the normal separation Δ_n for three

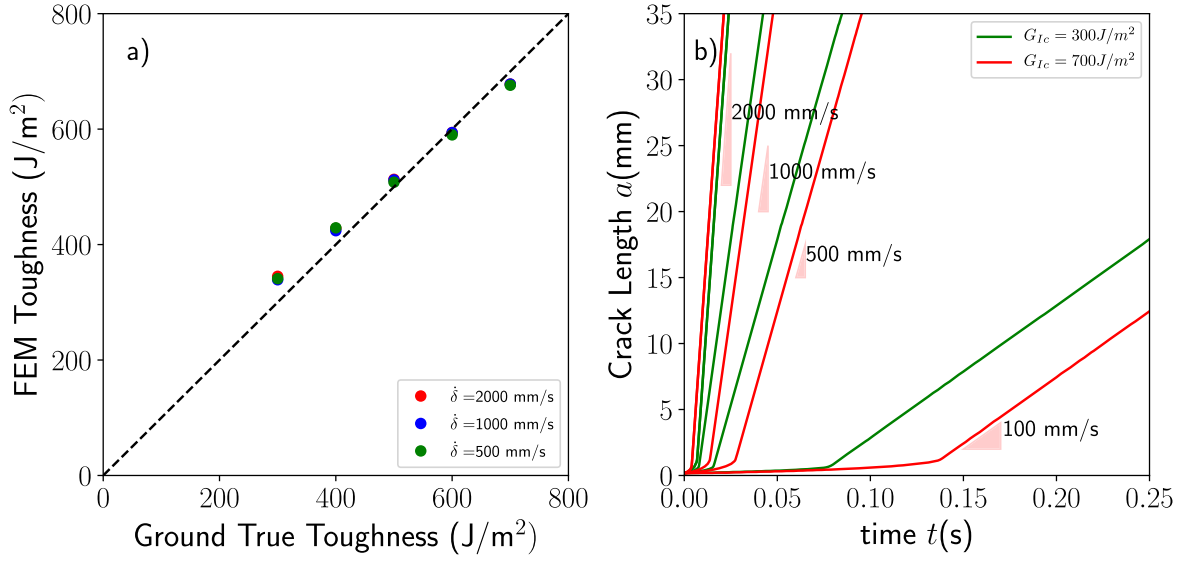

Fig. 10. (a) Relation between ground true fracture toughness G_{Ic} and FEM toughness obtained from maximum strain gauge readings ϵ_1 and ϵ_2 and expression (10), (b) time evolution of the crack length obtained for the different WIF displacement rates analyzed. (For interpretation of the references to color in this figure legend, the reader is referred to the web version of this article.)

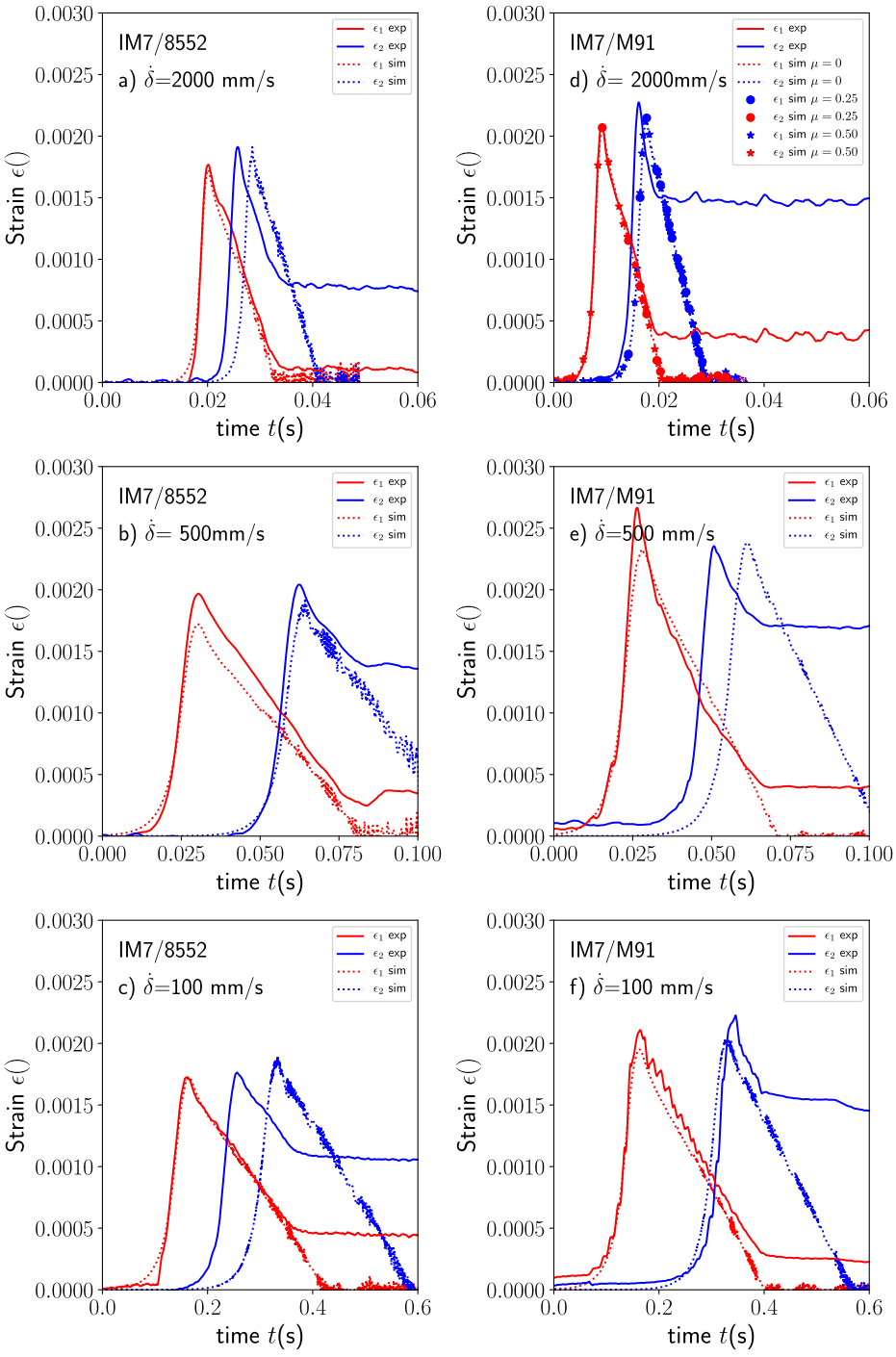

Fig. 11. Strain evolution curves corresponding to two strain gauges attached at 15 mm (ϵ_1) and 30 mm (ϵ_2) from the initial crack tip IM7/8552 and IM7/M91 specimens tested at $\dot{\delta}$ = 2000 mm/s, $\dot{\delta}$ = 500 mm/s and $\dot{\delta}$ = 100 mm/s displacement rates. A time shift was adjusted to the signals so start of the first strain gauge reading was the similar in both experiments and simulations. The effect of different pin/composite friction coefficients (μ = 0, 0.25 and 0.50) is illustrated in (d) for the IM7/M91 laminate tested at 2000 mm/s. (For interpretation of the references to color in this figure legend, the reader is referred to the web version of this article.)

representative cohesive elements located at the crack tip and at ≈ 15 mm and ≈ 30 mm from the crack tip is now represented by a WIF displacement rate of $\dot{\delta}$ = 2000 mm/s using the upper and lower limits of the fracture toughness of G_{Ic} = 300 J/m^2 and 700 J/m^2 in Fig. 12(a). It should be noted that the selected elements were located in the same beam section as the location as the strain gauges ϵ_1 and ϵ_2. The data obtained from the simulation was used to determine the normal separation rate $\dot{\Delta}_n$ at the two characteristic points in the softening curve namely the separation rate at the onset of fracture $\dot{\Delta}_{n0}$ and the separation rate for the fully damaged condition $\dot{\Delta}_{nc}$. These rate results, $\dot{\Delta}_{n0}$ and $\dot{\Delta}_{nc}$, were computed by the numerical derivative of the $t - \Delta_n$ points recorded from the simulations and superimposed by using dots and crosses in Fig. 12(a). From these results, it is shown that the normal separation rate was not constant in time with this value being smaller at the onset of fracture ($\dot{\Delta}_{n0}$) compared with the total separation condition ($\dot{\Delta}_{nc}$).

Not surprisingly, the separation rate $\dot{\Delta}_n$ measured for the elements located at ≈ 15 mm and ≈ 30 mm from the crack tip were very similar to

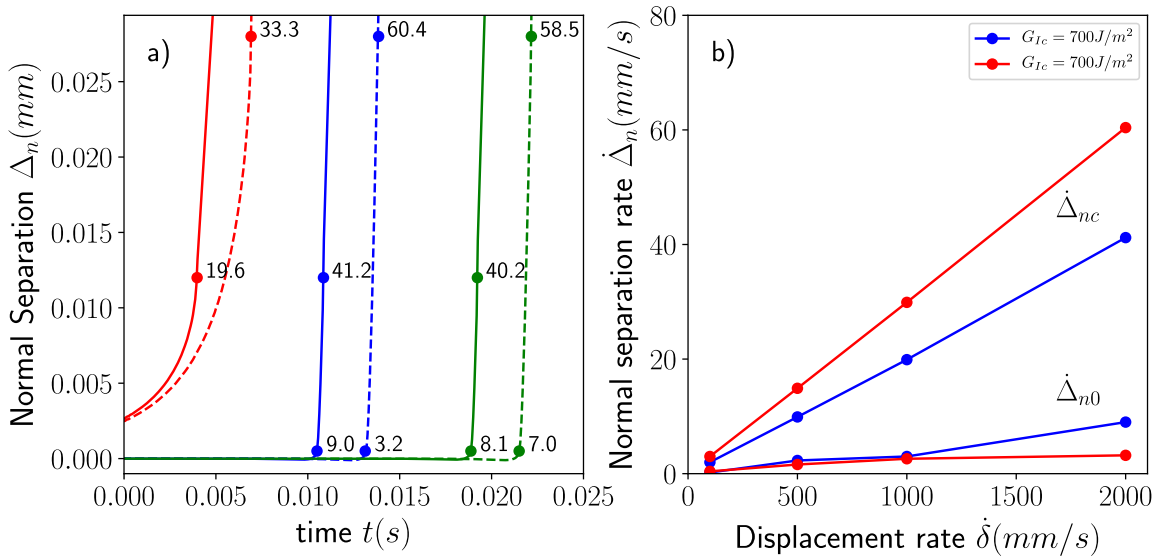

Fig. 12. (a) Time evolution of the normal separation Δ_n displacement for three equally spaced cohesive elements (crack tip and 15 and 30 mm from it) obtained from simulations using WIF displacement rate of $\dot{\delta} = 2000$ mm/s for: (a) $G_{Ic} = 300$ J/m^2 (solid line) and (b) $G_{Ic} = 700$ J/m^2 (dashed line). Dots represent the characteristic points of the softening curve corresponding to the onset of fracture $\Delta_{n0} = N/K$ while crosses indicate the final separation $\Delta_{nc} = 2G_{Ic}/N$. The accompanying number for each of the dots and crosses corresponded with the normal separation rate ($\dot{\Delta}_{n0}$ or $\dot{\Delta}_{nc}$) expressed in mm/s, (b) relationship between the normal separation rate, $\dot{\Delta}_{n0}$ and $\dot{\Delta}_{nc}$ of an element as a function of the WIF displacement rate applied $\dot{\delta}$. (For interpretation of the references to color in this figure legend, the reader is referred to the web version of this article.)

each other, indicating a self-similar propagation of the cohesive crack through the WIF sample (a simple time shift between the curves). This fact implies a requirement to install strain gauges far away from the initial crack tip.

Lastly, the relationship between the separation rate $\dot{\Delta}_n$ obtained from the finite element simulations and the corresponding WIF displacement rates $\dot{\delta}$ is now presented in Fig. 12(b) for the upper and lower limits of the fracture toughness of $G_{Ic} = 300$ J/m^2 and 700 J/m^2. As in previous results, see Fig. 7(a), the separation rate exhibited a linear dependence with respect to the applied WIF displacement rate $\dot{\delta}$ regardless of the fracture energy used in the simulations. In all the cases, significant differences between the normal opening rates $\dot{\Delta}_{n0}$ and $\dot{\Delta}_{nc}$ were observed for the cases analyzed. It should be noted that the finite element simulations carried out did not incorporate any rate dependence on the mechanical behaviour of either the cohesive elements or the bulk composite beams, as the aim was to study the WIF test rather than use it as a parameter identification method. A future rate dependence model for the cohesive behaviour should thus be implemented in terms of the inclusion of rate effects on both Δ_{n0} and Δ_{nc} (or N and G_{Ic}).

5. Conclusions

DCB and WIF specimens of IM7/8552 and IM7/M91 composite panels were prepared for characterisation of the mode I fracture toughness under dynamic conditions. Quasi-static loading conditions were also imposed in DCB specimens through use of an electromechanical testing frame with arm loading speeds $\dot{\delta}$ ranging from 0.5 to 450 mm/min. In the case of dynamic loading, a Gleeble 3800-GTC thermal-mechanical system was used instead which allowed the loading speeds between $\dot{\delta} = 100$ to 2000 mm/s to be imposed. DCB tests were used to characterize the fracture toughness for quasi-static conditions as well as the calibration curve for the specimen compliance required for the data reduction method used. As quasi-static tests carried out on longitudinal tensile coupons revealed no significant strain-rate dependence in this regime, it was assumed that the calibration compliance was independent of the loading rate. WIF specimens were instrumented with two strain gauges installed far from the crack tip (≈15 and 30 mm in the bending surfaces). The evolution of the strain was captured and the maximum value in compression was used to infer the corresponding toughness under dynamic conditions. In addition, the maximum strain-rate determined from the gauge signals was used to compare WIF and DCB tests under the same conditions (same abscissa axis).

The results revealed no rate dependence behaviour in mode I for the IM7/8552 while the IM7/M91 showed an increase at higher rates with a maximum peak at 500 mm/s. The fracture surface of IM7/M91 laminates exhibited different regions corresponding to the ductile tearing of the interleaved region probably triggered by particle debonding, while in the remaining surface fiber bridging and breakage were evident. It was assumed that the dynamic enhancement of the fracture behaviour in the interleaved region induced crack jump and diversion of the crack into the neighbor fiber ply, producing an additional toughening mechanisms in the form of ply bridging. This latter mechanism was also supported by X-ray computed tomography imaging. However, it is still unclear why IM7/M91 laminates showed an absolute fracture toughness peak in the range of displacement rates analyzed which seems to be more dependent on a fracture mechanisms competition rather than intrinsic strain-rate dependence.

A finite element model was prepared to understand the dynamic process during WIF testing. The method discretizes the laminate in two dimensions and cohesive elements are located at the interface between the beams of specimen. The WIF pin is displaced at constant rate given by the experiments and the crack advanced according to the loading conditions. No strain-rate effects were included in the model. The model was used to check the accuracy of the data reduction method proposed in Section 2. The strain gauge readings correlated reasonably well with the experiments, with the maximum values and time evolution shape being suitably captured. The maximum strain values were used to determine the toughness given by the model, which is in good agreement with the experimental results presented in this work. A second interesting result given by the model was the ability to estimate the crack separation rates that can be used as a rate indicator for the cohesive fracture. The separation displacement rate was computed by the numerical derivative of the normal separation displacement of the cohesive elements. It was shown that the separation rate was not constant either through the cohesive softening curve or the crack. At the onset of cracking, the displacement rate was much lower than the final failure condition because the loss of load-carrying capacity of the

cohesive element that is able to open faster than in the previous condition. In addition, the separation rates close to the initial crack tip were different. The crack speed requires a certain length to achieve the velocity imposed by the displacement pin while the cohesive crack moves in a self-similar way after this point.

Declaration of Competing Interest

The authors declared that there is no conflict of interest.

Acknowledgements

The research leading to these results has received funding from the European Union as Horizon 2020 research and innovation program under the Marie Sklodowska-Curie grant agreement No. 722096, DYNACOMP project.

References

[1] McMullen P. Fibre/resin composites for aircraft primary structures: a short history, 1936–1984. Composites 1984;15(3):222–30.
[2] Mangalgiri PD. Composite materials for aerospace applications. Bull Mater Sci 1999;22(3):657–64.
[3] Soutis C. Fibre reinforced composites in aircraft construction. Prog Aerosp Sci 2005;41(2):143–51.
[4] Kassapoglou Christos. Design and analysis of composite structures: with applications to aerospace structures. John Wiley & Sons; 2013.
[5] Sankar Bhavani. Low-velocity impact response and damage in composite materials. Key Eng Mater 1996;549–582(01):120–1.
[6] Segreto Tiziana, Teti Roberto, Lopresto Valentina. Non-destructive testing of low-velocity impacted composite material laminates through ultrasonic inspection methods. Characterizations of some composite materials. IntechOpen; 2018.
[7] Hong Seongho, Liu Dahsin. On the relationship between impact energy and delamination area. Exp Mech 1989;29(2):115–20.
[8] Friedrich K, Walter R, Carlsson LA, Smiley AJ, Gillespie JW. Mechanisms for rate effects on interlaminar fracture toughness of carbon/epoxy and carbon/peek composites. J Mater Sci 1989;24(9):3387–98.
[9] Davies GAO, Zhang X. Impact damage prediction in carbon composite structures. Int J Impact Eng 1995;16(1):149–70.
[10] Kusaka Takayuki, Hojo Masaki, Mai Yiu-Wing, Kurokawa Tomoaki, Nojima Taketoshi, Ochiai Shojiro. Rate dependence of mode i fracture behaviour in carbon-fibre/epoxy composite laminates. Compos Sci Technol 1998;58(3):591–602.
[11] Kusaka Takayuki, Kurokawa T, Hojo Masaki, Shojiro Ochiai. Evaluation of mode ii interlaminar fracture toughness of composite laminates under impact loading, vol. 141–143; 01 1998. p. 477–500.
[12] Benmedakhene S, Kenane M, Benzeggagh ML. Initiation and growth of delamination in glass/epoxy composites subjected to static and dynamic loading by acoustic emission monitoring. Compos Sci Technol 1999;59(2):201–8.
[13] Zabala H, Aretxabaleta L, Castillo G, Aurrekoetxea J. Loading rate dependency on mode i interlaminar fracture toughness of unidirectional and woven carbon fibre epoxy composites. Compos Struct 2015;121:75–82.
[14] Daniel IM, Yaniv G, Auser JW. Rate effects on delamination fracture toughness of graphite/epoxy composites. Netherlands, Dordrecht: Springer; 1987. p. 258–72.
[15] Aliyu AA, Daniel IM. Effects of strain rate on delamination fracture toughness of graphite/epoxy. Delamination and debonding of materials. ASTM International; 1985.
[16] Yaniv Gershon, Daniel Isaac M. Height-tapered double cantilever beam specimen for study of rate effects on fracture toughness of composites. Composite materials: testing and design (Eighth Conference). ASTM International; 1988.
[17] Kageyama K, Kobayashi T, Chou T-W. Analytical compliance method for mode i interlaminar fracture toughness testing of composites. Composites 1987;18(5):393–9.
[18] Smiley AJ, Pipes RB. Rate effects on mode i interlaminar fracture toughness in composite materials. J Compos Mater 1987;21(7):670–87.
[19] Blackman BRK, Dear JP, Kinloch AJ, Macgillivray H, Wang Y, Williams JG, et al. The failure of fibre composites and adhesively bonded fibre composites under high rates of test. J Mater Sci 1995;30(23):5885–900.
[20] Brunner AJ, Blackman BRK, Davies P. A status report on delamination resistance testing of polymer–matrix composites. Eng Fract Mech 2008;75(9):2779–94. Fracture of Composite Materials.
[21] You Hee, Yum Young-Jin. Loading rate effect on mode i interlaminar fracture of carbon/epoxy composite. J Reinf Plast Compos 1997;16(6):537–49.
[22] Sun CT, Han C. A method for testing interlaminar dynamic fracture toughness of polymeric composites. Compos Part B: Eng 2004;35(6):647–55. Marine Composites.
[23] May Michael. Measuring the rate-dependent mode i fracture toughness of composites – a review. Compos Part A: Appl Sci Manuf 2016;81:1–12.
[24] Thorsson Solver I, Waas Anthony M, Schaefer Joseph, Justusson Brian, Liguore Salvatore. Effects of elevated loading rates on mode i fracture of composite laminates using a modified wedge-insert fracture method. Compos Sci Technol 2018;156:39–47.
[25] Jacob George C, Michael Starbuck J, Fellers John F, Simunovic Srdan, Boeman Raymond G. The effect of loading rate on the fracture toughness of fiber reinforced polymer composites. J Appl Polym Sci 2005;96(3):899–904.
[26] Cantwell Wesley J, Blyton M. The interlaminar fracture properties of composite materials at high rates of strain. Impact response and dynamic failure of composites and laminate materials. Key engineering materials, vol. 141. Trans Tech Publications Ltd; 1997. p. 463–76.
[27] Whitney JM, Browning CE, Hoogsteden W. A double cantilever beam test for characterizing mode i delamination of composite materials. J Reinf Plast Compos 1982;1(4):297–313.
[28] Hojo Masaki, Kageyama Kazuro, Tanaka Kiyoshi. Prestandardization study on mode i interlaminar fracture toughness test for cfrp in Japan. Composites 1995;26(4):243–55.
[29] Ponnusami Sathiskumar A, Cui Hao, Erice Borja, Pathan Mehtab V, Petrinic Nik. A wedge-dcb test methodology to characterise high rate mode-i interlaminar fracture properties of fibre composites. EPJ Web Conf 2018;183:02052.
[30] Czabaj Michael W, Ratcliffe James G. Comparison of intralaminar and interlaminar mode i fracture toughnesses of a unidirectional im7/8552 carbon/epoxy composite. Compos Sci Technol 2013;89:15–23.
[31] Savitzky Abraham, Golay MJE. Smoothing and differentiation of data by simplified least squares procedures. Anal Chem 1964;36(8):1627–39.